5-2021

Development of a Variable Extensometer Method for Measuring Ductility Scaling Parameters

Adam J. Smith
Utah State University

DEVELOPMENT OF A VARIABLE EXTENSOMETER METHOD FOR MEASURING DUCTILITY SCALING PARAMETERS

by

Adam J. Smith

A thesis submitted in partial fulfillment
of the requirements for the degree

of

Master of Science

in

Mechanical Engineering

Approved:

Ryan B. Berke, PhD Major Professor	Thomas Fronk, PhD Committee Member
Juhyeong Lee, PhD Committee Member	D. Richard Cutler, Ph.D. Interim Vice Provost of Graduate Studies

UTAH STATE UNIVERSITY
Logan, Utah

2021

ABSTRACT

Development of a Variable Extensometer Method for Measuring Ductility Scaling Parameters

by

Adam J. Smith, Master of Science

Utah State University, 2021

Major Professor: Dr. Ryan Berke
Department: Mechanical and Aerospace Engineering

Ductility is a vital material property for understanding the design life and thermo-mechanical behavior of nuclear components. Components inside nuclear systems and reactors are regularly exposed to both radiation and high, fluctuating temperatures. Temperature has a large impact on the ductility of a material, and radiation contributes to embrittlement. Both responses are dependent on radiation dose, and therefore it is necessary to characterize ductility at multiple different temperatures and radiation doses. However, testing of irradiated materials introduces numerous logistical and safety concerns. To mitigate this, measurements are often made on nano- and micro-scale specimens, which are easier to handle and require less total radiation. These small-scale techniques do not necessarily capture a material's behavior at an engineering scale, and thus there is a need to translate ductility measurements to the macro-scale.

Macro-scale ductility is not an intrinsic material property but is also dependent on the overall geometry of the specimen. To account for variety in specimen geometries, multiple ductility scaling laws have been developed which scale ductility between different

specimen sizes. Traditionally, these rely on testing multiple different specimens of varying sizes to obtain material parameters, often done by varying gauge lengths. With the use of Digital Image Correlation (DIC), this work explores a technique where multiple different gauge lengths are extracted from a single specimen to obtain ductility scaling parameters. This technique provides orders of magnitude more data from each specimen than previous techniques. This technique was validated through the testing of multiple different geometries and a comparison of different scaling laws was made.

(61 pages)

PUBLIC ABSTRACT

Development of a Variable Extensometer Method for Measuring Ductility Scaling Parameters

Adam J. Smith

Ductility is the measure of how much a material can stretch before separation. It is usually measured in percent elongation, which is the amount a material stretches divided by its original length before stretching. This is an important property to understand for both the design for performance and safety. A material's ductility can be influenced by several factors including heat treatment, machining, temperature, and radiation dose. Materials used in nuclear energy facilities are often exposed to all these factors, and it is important to be able to understand ductility at each possible combination.

Ductility is usually characterized through tension tests where a material is stretched until separation and the percent elongation is measured. However, ductility measured this way is dependent on the specimen geometry, meaning specimens of different lengths and thicknesses of the same material produce different percent elongation values. To account for this, ductility scaling laws have been developed that scale percent elongation to specimens of different sizes. Traditionally, these laws require testing multiple different specimen geometries to empirically extract the scaling parameters. This can be cost-prohibitive for many materials used for nuclear energy. This work develops a technique for extracting scaling parameters from a single specimen with the use of Digital Image Correlation—a camera-based measurement that extracts displacements from the pixel data

across the entirety of the specimen. Improvements to the current scaling laws have been proposed, and the technique is validated by testing specimens of multiple different geometries.

ACKNOWLEDGMENTS

I would firstly like to give special thanks to my advisor Dr. Ryan Berke. His help presenting and exploring research ideas, troubleshooting problems, and with numerous writing reviews was absolutely instrumental throughout the entire process. I would not have been able to do it without his guidance. I would also like to thank my committee members Dr. Thomas Fronk and Dr. Juhyeong Lee for their continued support and assistance.

Additionally, I would like to thank my colleagues, friends, and family for their helpful ideas, encouragement, and moral support. Lastly, I would like to thank the Department of Energy Nuclear Energy University Program for funding my research.

Adam J. Smith

CONTENTS

Page

LIST OF TABLES

LIST OF FIGURES

CHAPTER 1

INTRODUCTION

1.1 Ductility Scaling Laws

As nuclear facilities age, it is critical to understand how materials degrade under irradiation conditions [1]. However, engineering-scale radioactive specimens are expensive to irradiate and difficult to handle [2]. A common area of concern for irradiated materials is the effect of reduced ductility [3]. So, there is a strong desire to develop techniques that can adequately characterize the effect of irradiation on ductility. Traditionally, ductility characterization is performed using engineering scale tensile tests. However, testing of high-temperature and irradiated materials with this technique can present numerous safety and logistical challenges [2]. As such, there is significant interest in low cost methods to characterize the ductility of materials. A common method is using miniaturized specimens, which experience less total radiation dose and are much safer to handle [4]. In recent years, several promising techniques have gained popularity (for example: nano-indentation [5–7], Micro-electro-mechanical-system based micro-tension [8–10], nano-pillar compression [11,12], or disk bend [2]). These techniques focus on measurements at a micro- or nano-scale and avoid macro-scale instrumentation. This has led to a significant gap in translating measurements at a micro- or nano-scale to material properties at an engineering scale.

Among other phenomena, ductility is affected by grain size [13–15], temperature [16,17], and total radiation dose [18,19]. To understand how nuclear components will perform, it is necessary to characterize the ductility for each combination of environmental

factors. However, ductility is also dependent on specimen geometry [20–23]. For example, in the late stages of ductility testing, localized necking means that two specimens of differing dimensions can produce drastically different elongation measurements [24]. So, it is necessary to use scaling laws to translate ductility measurements between different sized specimens. One of the first, Barba's Law, shown in eq. 1, was developed in 1880 [25].

$$e_f = \beta \frac{\sqrt{A_0}}{L_0} + e_u \tag{1}$$

Where e_f is the total elongation at failure (units of strain), A_0 is the initial specimen area (units of length^2), and l_0 is the initial specimen length. β and e_u are scaling parameters where e_u represents the total uniform elongation (units of strain) and β is a coefficient that represents the necked region (unitless). Traditionally, Barba's Law parameters (β and e_u) are found by testing multiple specimens of the same material having different combinations of area and length, then fitting a linear equation to the data. Figure 1 shows an example of this process where the slope of the line is β and the y-intercept is e_u. Under a limited range of geometries, this equation provides a reasonable estimate, but the phenomenon is not entirely linear.

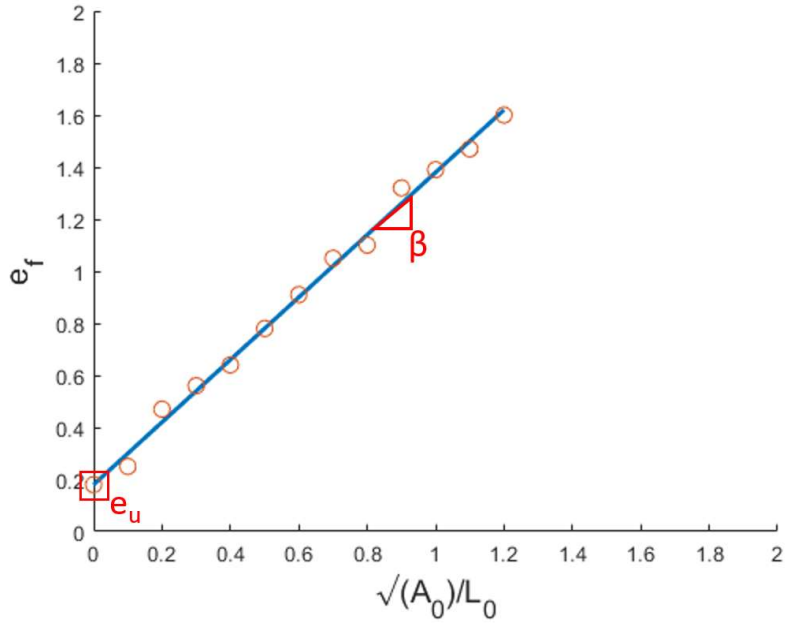

Figure 1. An example of Barba's Law using example data. The slope, β, and the y-intercept, e_u, are clearly labeled

In 1928, Oliver showed that the distribution for total elongation versus the inverse of the gauge length did not follow a straight line over a wide range of values. However, plotting percent elongation vs. the gauge length (L_0) on a logarithmic scale produced a straight line. Following the example from Barba's Law, he modified the horizontal parameter to include the aspect ratio L_0/sqrt(A_0). This lead to the development of Oliver's Law shown in eq. 2 [26]. κ represents the y-intercept on a log scale and α describes the slope.

$$e_f = \kappa \left[\frac{L_0}{\sqrt{A_0}}\right]^{\alpha} \tag{2}$$

An example of Oliver's Law can be seen on a linear scale in Figure 3a and on a logarithmic scale in Figure 3b. This equation allows for curvature that better can represent the data and scales between geometries, but Oliver's Law parameters are less intuitive when applying to engineering problems. Examining Barba's Law, the uniform elongation is found when sqrt(A_0)/L_0 goes to 0 or when gauge length becomes infinitely long, and the non-uniform elongation becomes negligible. Using Oliver's Law at longer and longer gauge lengths, e_f will decay to zero instead of the expected uniform elongation.

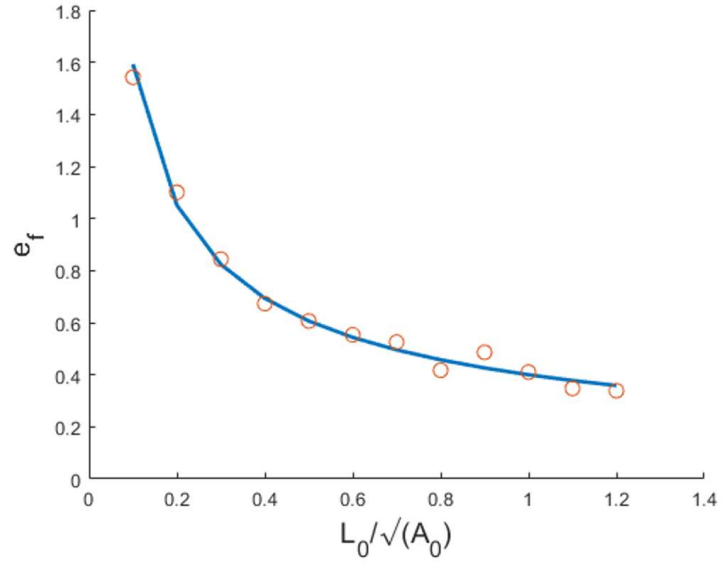

(a)

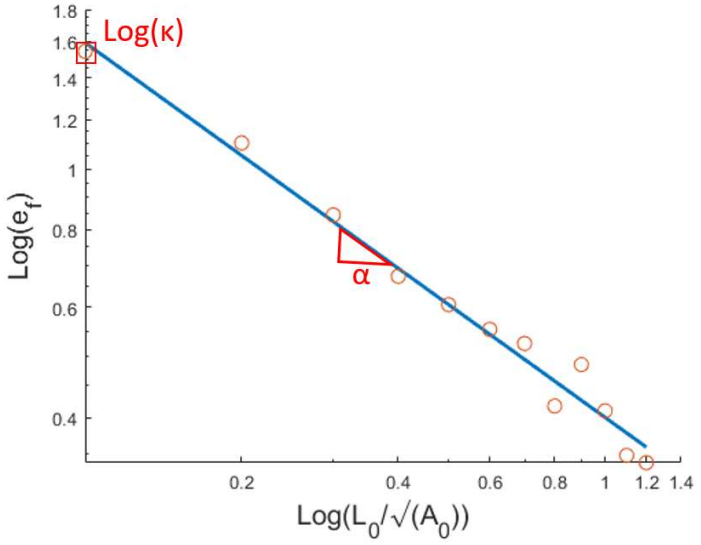

(b)

Figure 2. Oliver's Law plotted from example data on (a) a linear scale and (b) a logarithmic scale with α and κ labeled

Oliver's Law has become the standard scaling law used in ISO 2566-1:1984 [27]. Although, it does have limitations. Takeda et al. demonstrated that Oliver's Law is not applicable to pure iron with a thickness between 0.2 mm and 2 mm, due to the effect of stress triaxiality [20]. Chen et al. verified the applicability of both Oliver's and Barba's Law if the specimen aspect ratio was less than or equal to 9.89. The ISO 2566-1 states that Oliver's Law is not applicable to steels with a tensile strength over 700 MPa. However, Xu et al. addressed this by developing modifications to Oliver's Law for the use on high-strength pipeline steel by adding a term that was dependent on tensile strength [28].

Both Oliver's and Barba's Law require testing multiple specimens of different geometries to empirically obtain the ductility scaling parameters (β and e_u, or κ and α). This can be expensive and introduce safety hazards when testing high-temperature or irradiated specimens. One method to combat this was developed by Dhalla and Winter [29]. With the observation that the only criterion for L_0 is that it must encase the non-uniform elongation (i.e. necking), they marked multiple gauge lines every ¼" along a 3" specimen, shown in Figure 3. By measuring the total elongation between each gauge line post-mortem, they were able to obtain both Barba's Law and Oliver's Law parameters from a single specimen, thus reducing cost and time while improving safety. In this work, their technique is expanded upon through the development of a novel variable extensometer method to obtain ductility parameters using Digital Image Correlation (DIC).

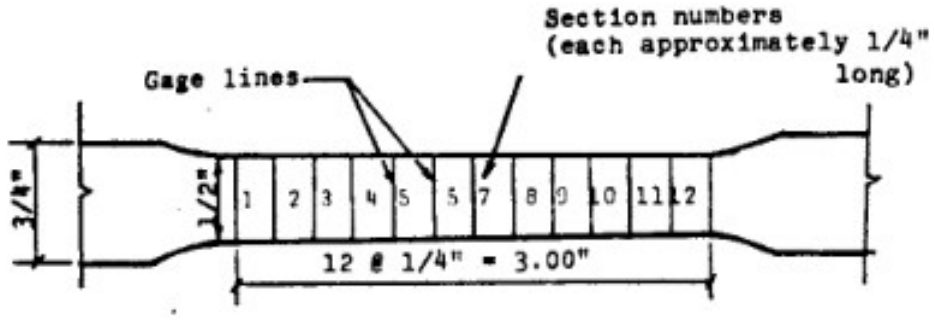

Figure 3. A diagram taken from the work by Dhalla and Winter demonstrating their technique for extracting scaling parameters from a single specimen [29].

1.2 Overview of Digital Image Correlation

Digital Image Correlation (DIC) is an image-based displacement measurement technique, which offers several unique benefits. First, it is a non-contact method capable of in-situ measurements [30]. Second, it can be applied to different length scales limited only by the field-of-view and resolution of the camera [31]. Lastly, it provides full-field data across the entirety of the specimen surface as opposed to the single point strain of strain gauge or the total extension of a physical extensometer [32]. These benefits make it an excellent technique for extracting multi-scale ductility data from an in-situ tension test.

DIC uses a series of images taken before and after deformation. The first image taken is the reference image to which all other images are compared. However, because each image contains many more pixels than there are unique values for each pixel to take, instead of tracking individual pixels across images the DIC algorithm tracks subsets of multiple pixels. Each subset is a pixel by pixel square area which the DIC software uses to track unique features over the course of deformation. These features need to be high contrast and must be sized appropriately for the camera resolution and specimen sizes [33].

This is commonly done be applying random paint droplets—referred to as a speckled pattern—onto a high contrast background. Each displacement measurement is computed across the entire subset of pixels [34]. The subset size is a controllable parameter, as is the step size (meaning the distance from the center of one subset to the center of another neighboring subset). By selecting a step size that is smaller than the subset size, neighboring subsets can overlap.

Speckle size, subset size, and length scale are all important factors to consider when performing DIC measurements. For each subset to be properly identified by the DIC algorithm, the speckle pattern must be random, non-repeating, and isotropic [35]. The speckle size should not be too small as to be indistinguishable with respect to the image resolution, but it should not be too large, or a single feature may dominate an entire subset [34]. The displacement is averaged over the entire subset; DIC with a smaller subset size produces more data points with a finer measurement resolution but is more sensitive to error. A larger subset size averages the measurement over a larger area reducing the ability to identify small length scale localization but will reduce uncertainty [36,37]. In summary, it is important to consider desired length scale, camera resolution, speckle size, and subset size when conducting DIC measurements.

There are many different ways to use DIC. Most commonly used is 2D DIC which measures in plane deformation on a flat surface from a single camera from a single camera. 3D DIC requires the use of two cameras and can measure both in plane and out of plane deformation on a surface [38]. Volumetric DIC—also known as digital volume correlation—is an imaging technique that applies the principles of DIC to x-ray or ultra-sound measurements to full-field 3D deformations [39]. Another way DIC has been used

is through the use of virtual extensometers. These are extensometers applied via DIC that track extension between two points on a specimen, which is tracking the displacement between two fixed subsets. This method is offered through a product called VIC-Gauge by Correlated solutions and has been used to characterize the ductility of additive manufactured materials [40]. This product is meant for measurements to be taken in real time. The measurements used for the variable extensometer method are taken after the fact. Thus, the Vic-Gauge product is not used in this work, but the virtual extensometer concept is extracted from 2D DIC data.

1.3 Overview

In this work, a novel variable extensometer approach was developed using DIC for the application to Barba's and Oliver's Law. By using many virtual extensometers—extracted manually from 2D DIC data—across the length of the specimen, multiple different initial lengths can be extracted from a single specimen, allowing for the determination of ductility scaling parameters. In this study, low carbon steel dog-bone tensile specimens with gauge lengths of 80 mm, 60 mm, and 40 mm were tested and compared for the validation of the technique. This document outlines the objectives of this work, methods used to meet objective, and their results and discussion.

CHAPTER 2

OBJECTIVES

1. Develop a technique for extracting Barba's and Oliver's Law parameters from a single specimen using DIC
2. Validate the technique through the comparison of multiple different specimen geometries
3. Compare the performance of Barba's and Oliver's Law and their ability to fit large data from a single specimen

CHAPTER 3

METHODS

3.1 Experimental Setup

Specimens were machined out of low carbon A36 steel sheet 2.5 mm thick with a constant 10 mm gauge width (A_0=25mm) using a CNC water jet with dimensions shown in Figure 4. Specimens were speckled with VHT High Temperature spray paint with a white background and a black speckle.

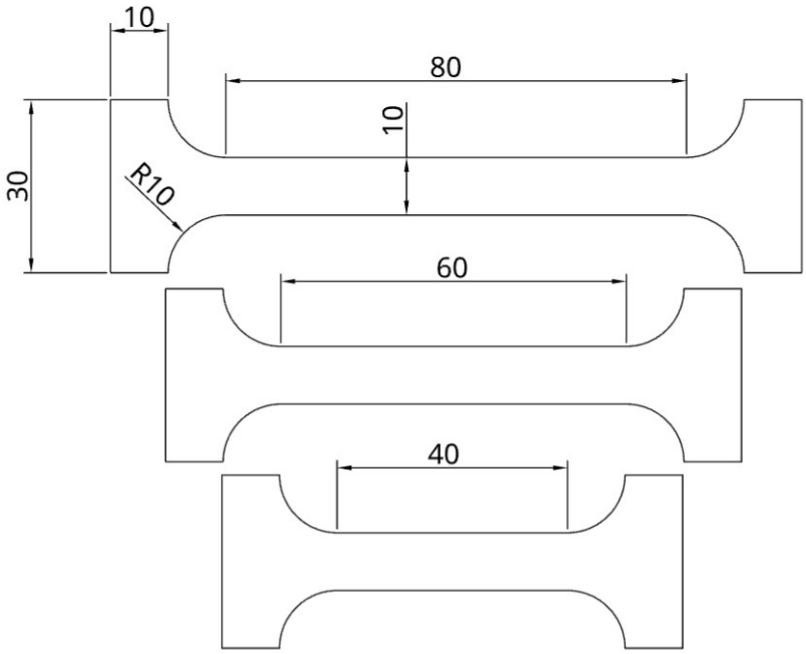

(a)

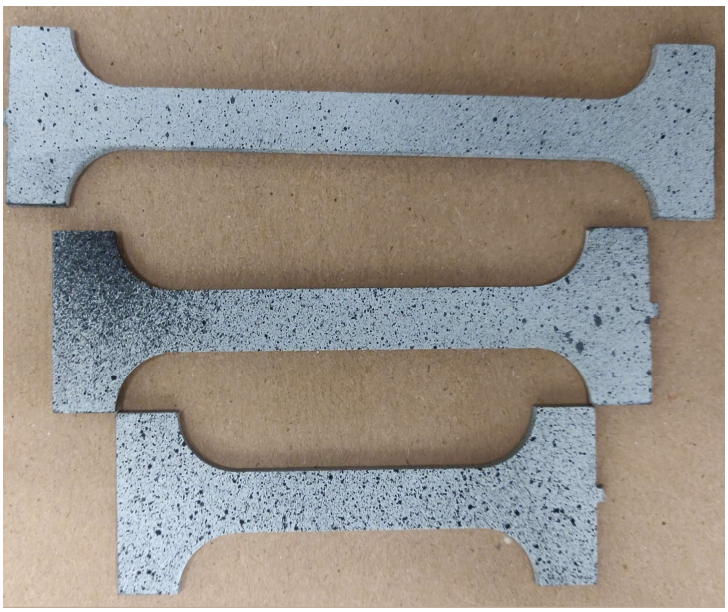

(b)

Figure 4. (a) Drawing of tensile specimens with 80 mm, 60 mm, and 40 mm gauge lengths used for testing (b) picture of a speckled specimens

A Gleeble 1500D thermomechanical simulator, which consists of a load frame with a joule heater inside of an environmental chamber, was used for testing. The environmental chamber of the Gleeble includes a viewing window through which to allow for image-based measurements to be taken during testing. To match the angle of the viewing window, specimens were placed in stainless steel grips machined at an angle that matches the window. The grips contain a recess that matches the shoulders of the specimen and the top half of the grips clamp down on the top with two ¼-20 bolts shown in Figure 5. The grip-to-grip displacement was measured using a Linearly Varying Displacement Transducer (LVDT).

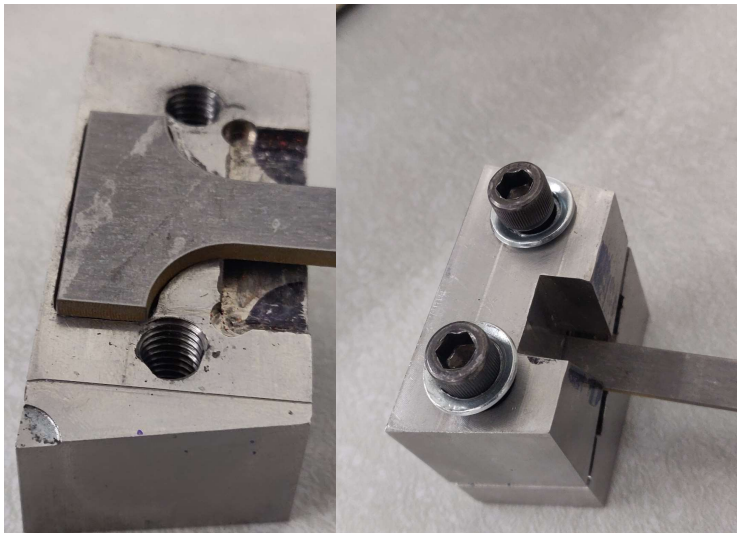

(a) (b)

Figure 5. (a) shows the specimen seated in the machined recess in the grips and (b) shows the top part of the grip that clamps onto the specimen and holds it in place. The grips angle the specimen to match the viewing angle of the Gleeble window. A notch was machined out of the grips to allow a view of the entire gauge length

The specimens were additionally monitored throughout testing by use of a 15.1 MP Basler (Exton, PA, USA) ace camera equipped with a 25 mm fused quartz lens from Universe Kogaku (Oyster Bay, New York, USA). Figure 6 displays this setup. Specimens were pulled under displacement control at a rate of 0.125 mm/s until fracture. Images were captured at a rate of 2 HZ during of the test. DIC was performed using Vic-2D v.6.2.0, a digital image correlation software from Correlated Solutions (Irmo, SC, USA) with a subset size of 125x125 pixels and a step size of 5 pixels.

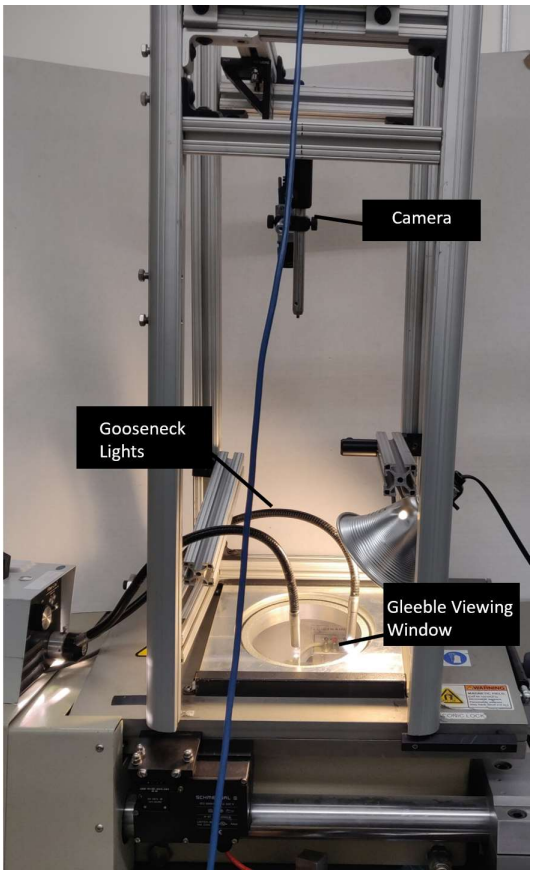

Figure 6. Camera and gooseneck lights setup over the Gleeble viewing window used to take images

3.2 Processing DIC Results

The DIC data was processed through several steps to extract the variable extensometer data. First, the neck regions was identified by examining the vertical and horizontal displacement along the length of the specimen detailed in 3.2.1. Then many different virtual extensometers were applied along the length of the specimen to extract the data, detailed in 3.2.2.

3.2.1 Identifying the Necked Region

The first step in this process is to find the pixel location of the necked region along the length of the specimen. This was accomplished through examination of both the horizontal and vertical displacement throughout the length of the specimen. The y-component of displacement (v) obtained from an 80 mm specimen is shown as a colormap in Figure 7a and plotted as a function of y-position in Figure 7b. In the necked region, the vertical displacement v(y), shown in Figure 7b, has a rapid increase in slope as the necked area displaces more drastically than the rest of the specimen. The slope of this curve, dv/dy shown in Figure 7c, clearly highlights the necked region. Figure 7d shows the horizontal displacement du/dx, obtained through a rolling average for each row of subsets, along the length of the specimen. The maximum value of dv/dy after the onset of necking serves as a good metric for the location of the necked region, and du/dx allows for validation of the location.

When applying virtual extensometers to study necking, it is important not to use extensometers that overlap with the necked region as that would introduce error into the results. To avoid this, a “dead zone," where subsets are ignored in the calculation, is

applied. The applied dead zone is 150 pixels on either side of the break along the length of the specimen, corresponding to 30 overlapping DIC subsets separated by the step size of 5 pixels. Since 150 is the distance to the center of the nearest 125x125 subset, this means that greater than 85 pixels on both sides of the break are excluded which excludes the neck from the subsets too.

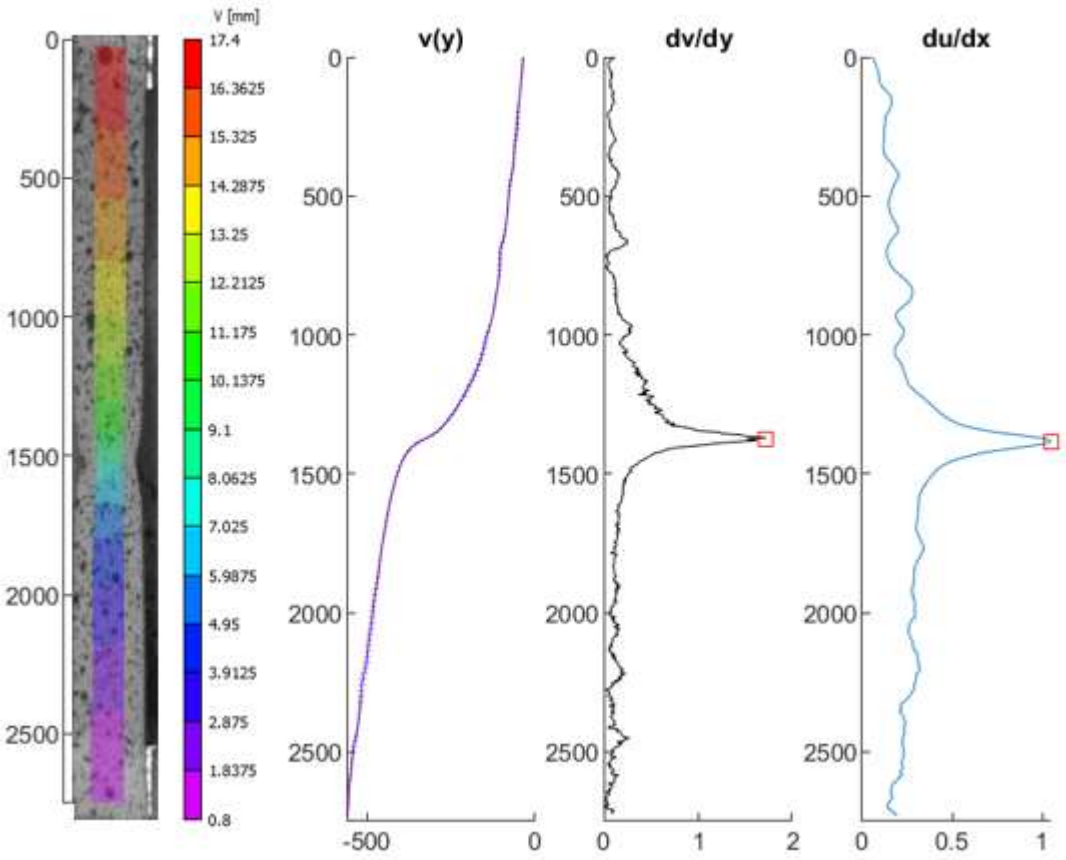

(a) (b) (c) (d)

Figure 7. Plots used for identifying the necked region. (a) the DIC contour giving of the vertical displacement in mm (b) the vertical displacement in terms of pixels v(y) along the length of the specimen (c) the change in vertical displacement along the length of the specimen and (d) the change in horizontal displacement du/dx across the width of the specimen

3.2.2 Applying Virtual Extensometers

To reduce the amount of noise in each measurement, the vertical displacement is averaged across each row of subsets along the width of the specimen. A row above the break is compared to a row below the break forming a single extensometer. This is then done for every combination of rows of subsets above and below the break, excluding the dead zone. The initial distance between the two points of the extensometer is L_0 and the difference between the displacement of the two points is ΔL, allowing for many calculations of elongation $\Delta L/L$ over time. The elongation at failure provides e_f. Figure 8 demonstrates this process.

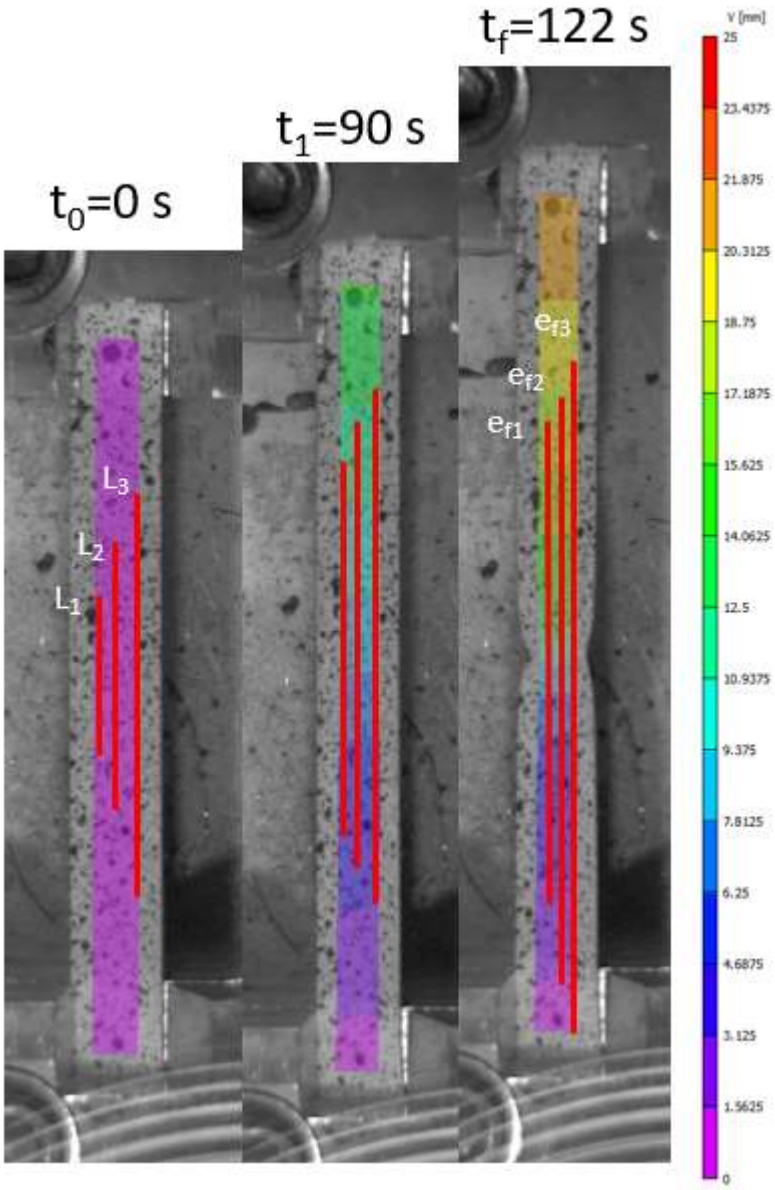

(a) (b) (c)

Figure 8. A diagram of the process used in step 2. (a) initial starting gauge lengths are obtained from the reference image, (b) the displacement for each starting length is tracked over the course of the tension test, and (c) the final elongation, e_f, is obtained just prior to specimen separation to

3.3 Generating Scaling Parameters

With the extensometer values extracted, the Matlab "fit()" function is used to fit equations 1, 2 and a third equation detailed in 3.4 extract the ductility parameters. An example of the variable extensometer method on a 60 mm specimen is applied to Barba's Law in Figure 9a and Oliver's Law in Figure 9b. In both figures, the total elongation of each extensometer, ef, is plotted against the geometry of the specimen – sqrt(A_0)/L_0 for Barba's Law or L_0/sqrt(A_0) for Oliver's. This demonstrates the ability of the technique to extract scaling parameters from a single specimen. In comparison with traditional techniques (Figures 1-2), this provides much more data points that aids in refining the equation fit.

Both equations are linear approximations. Barba's Law is in linear space and Oliver's is in logarithmic space. However, the data does not appear to follow a strictly linear trend. The linear equations do not properly characterize the smallest gauge lengths—large sqrt(A_0)/L_0 in Barba's Law or small L_0/sqrt(A_0) in Oliver's Law, as circled in Figure 9.

Of the two laws, Barba's Law includes a physically intuitive parameter, e_u, representing the value of e_f as the gauge length approaches infinity and the necked region contributes negligibly to elongation. This parameter has physical implications for the ability to scale micro- and nano-scale ductility measurements it up to any engineering-scale gauge length. Oliver's Law does not have a parameter to scale the uniform elongation and mathematically, e_f goes to zero at infinite gauge lengths.

However, one drawback of Barba's Law is that it insufficiently captures the shape of the data for small gauge lengths in linear space, as indicated by the circled region in

Figure 9a. Oliver's Law better fits this data in Figure 9b due to its use of an exponent, α. Despite better fitting the shape of the curve, Oliver's Law still fails to fit the data at some of the smallest gauge lengths, as indicated by the circular region in Figure 9b.

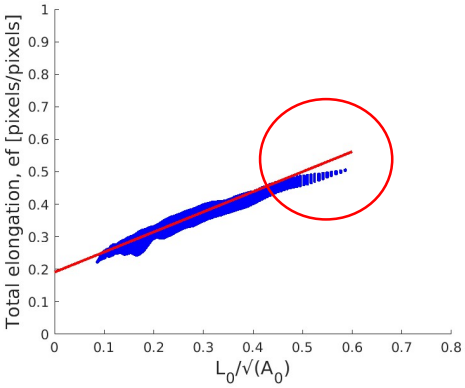

(a)

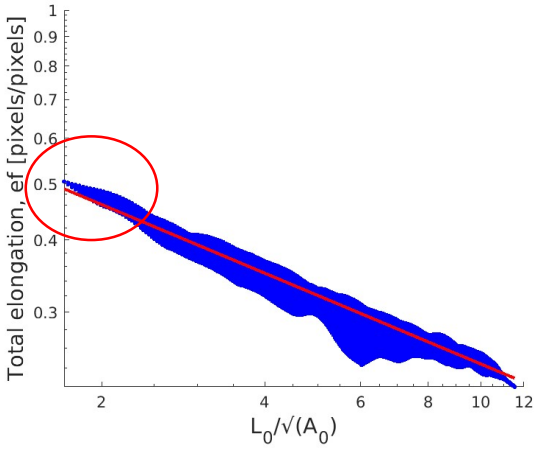

(b)

Figure 9. Variable extensometer data (a) shows e_f vs sqrt(A_0)/L_0 with Barba's Law equation fit overlayed on top (b) shows e_f vs L_0/sqrt(A_0) with Olivers's Law equation fit overlayed on top in log space

3.3.1 Unifying the Laws

As an analytical tool for comparing the two laws, a unified law is shown in equation 3:

$$e_f = \kappa \left[\frac{L_0}{\sqrt{A_0}}\right]^{\alpha} + e_u \tag{3}$$

This equation is similar to both Oliver's and Barba's Law. From the perspective of Oliver's Law, the modification is the addition of e_u. This changes the behavior of the law at infinite gauge lengths. Now, e_f will decay to e_u as L_0 goes to infinity. This provides a physically intuitive parameter that can scale up to specimens of any length. It also allows the κ and α parameters to better fit the more extreme curvature at smaller values of L_0. From the perspective of Barba's Law, there is an addition of the α exponent, which if set to negative one, yields the original Barba's Law equation. By introducing this parameter, the unified law can better capture the curvature of the data that cannot be done with a linear equation. For comparison purposes, Barba's Law will use κ instead of β with α set to negative one.

Each of these three functions was applied to the extensometer data using the Matlab "fit()" function. An example of the data extracted from a 60 mm specimen is shown applied to Barba's Law (Figure 9a), Oliver's Law (Figure 9b,c), and the Unified Law (Figure 10).

Three specimens with a 40 mm gauge length, three specimens with a 60 mm gauge length, and three specimens with an 80 mm gauge length were tested. The variable extensometer technique was applied to each specimen, and Barba's Law, Oliver's Law, and the Unified Law were applied to the extensometer values. This allows for a

comparison between all three laws and provides a validation by comparing parameters obtained through specimens of varying geometries.

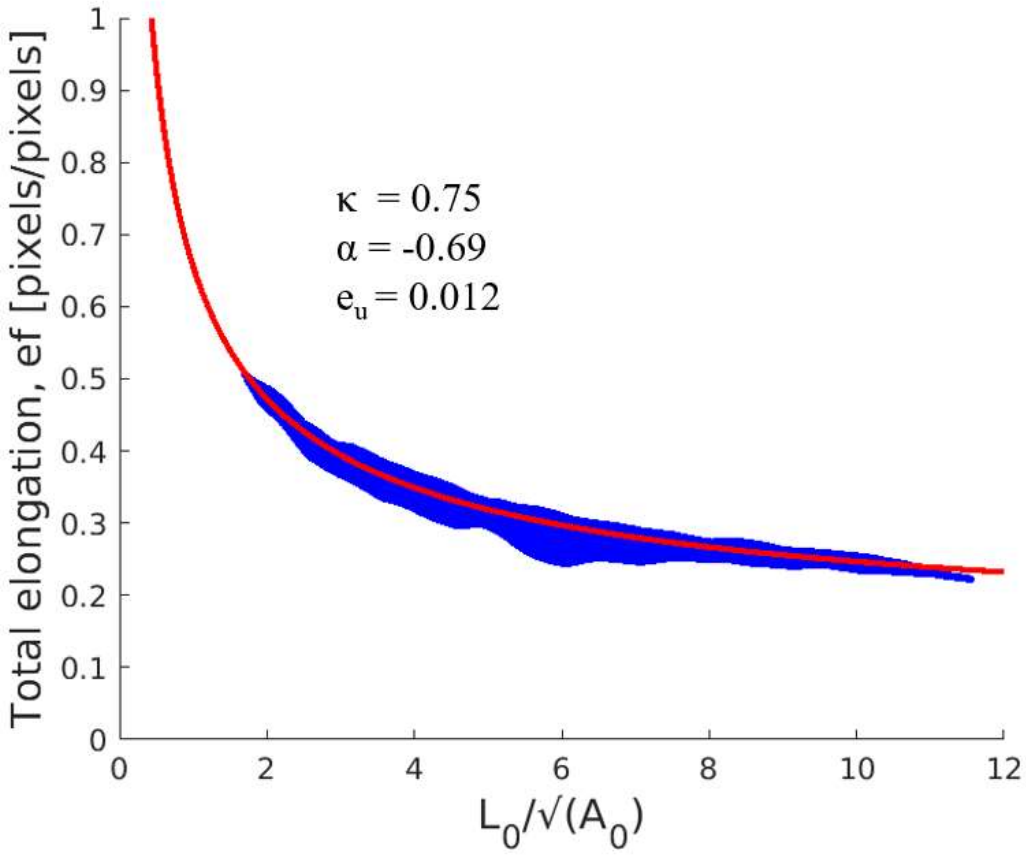

Figure 10. Extensometer data taken from the same 60 mm specimen as Figure 9 with the applied fit of the Unified Law

CHAPTER 4

RESULTS

4.1 Traditional (Non-Variable Extensometer) Method

As a benchmark, the variable extensometer method is compared to the more historically used technique recommended in in ISO 2566-1:1984 [27]. Under the technique, a single specimen-averaged measurement is obtained from each specimen, and ductility parameters are computed by fitting curves to the results of all 9 specimens. This is done by extracting final elongations using DIC taking the outermost valid extensometer value from each specimen along with the corresponding initial gauge length. These represent a single data point for each specimen. Each data point is then plotted on a common axis and the Matlab “fit()” function is then applied to this data to generate non-variable extensometer scaling parameters. This process is shown in Figure 11.

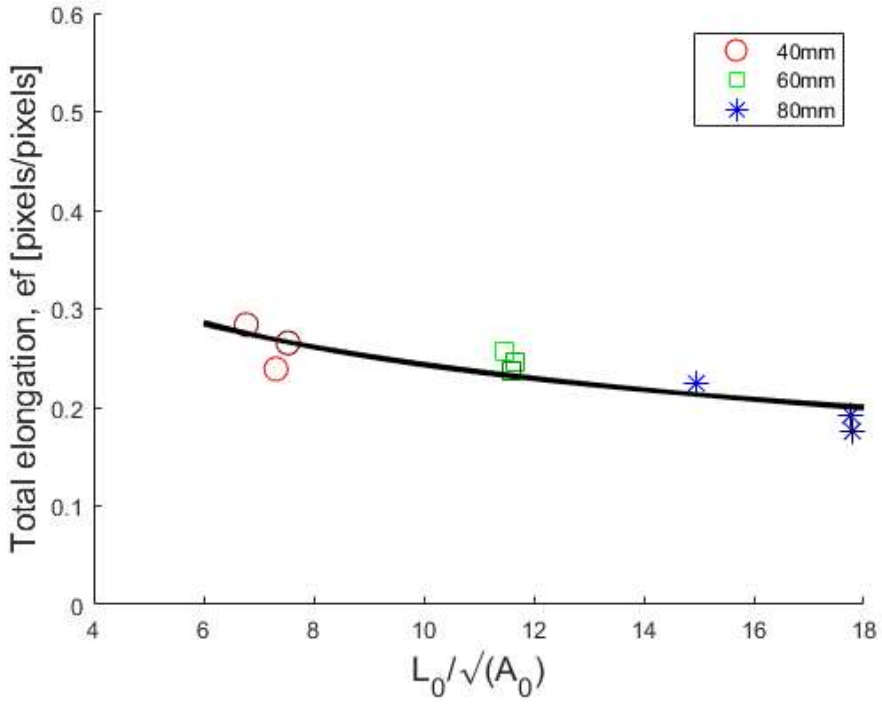

Figure 11. Data from each 40 mm, 60 mm, and 80 mm specimen taken from the non-variable extensometer technique with the fitted equation of the Unified Law overlayed

4.2 Combining the Data

The variable extensometer technique is not only applied independently to all 9 specimens but is also applied a 10th time to the entire data set resulting from all 9 specimens. The extensometer data for each specimen immediately prior to failure was plotted on a common axis. Using the entire combined dataset, each scaling law was applied to obtain scaling parameters for each scaling law. The combined data set is shown in Figure 12. For visible clarity, the 40 mm data set is plotted first in red, the 60 mm in green, and the 80 mm in blue. The gray data represents the other two specimen sizes in each plot. The data points used in Figure 11 are also shown on top of this data. This figure provides a visual indication of the variations in the variable extensometer

obtained between specimens. There exists a variation between specimens of different geometries, but it is comparable to the variation between specimens of the same geometry.

Examination of the traditional data on Figure 12 shows that specimens of the same geometry produce comparable final elongation values. Yet, there is a large distribution in the full behavior the data sets. This indicates that the outermost final elongation does fully characterize the deformation behavior of each specimen.

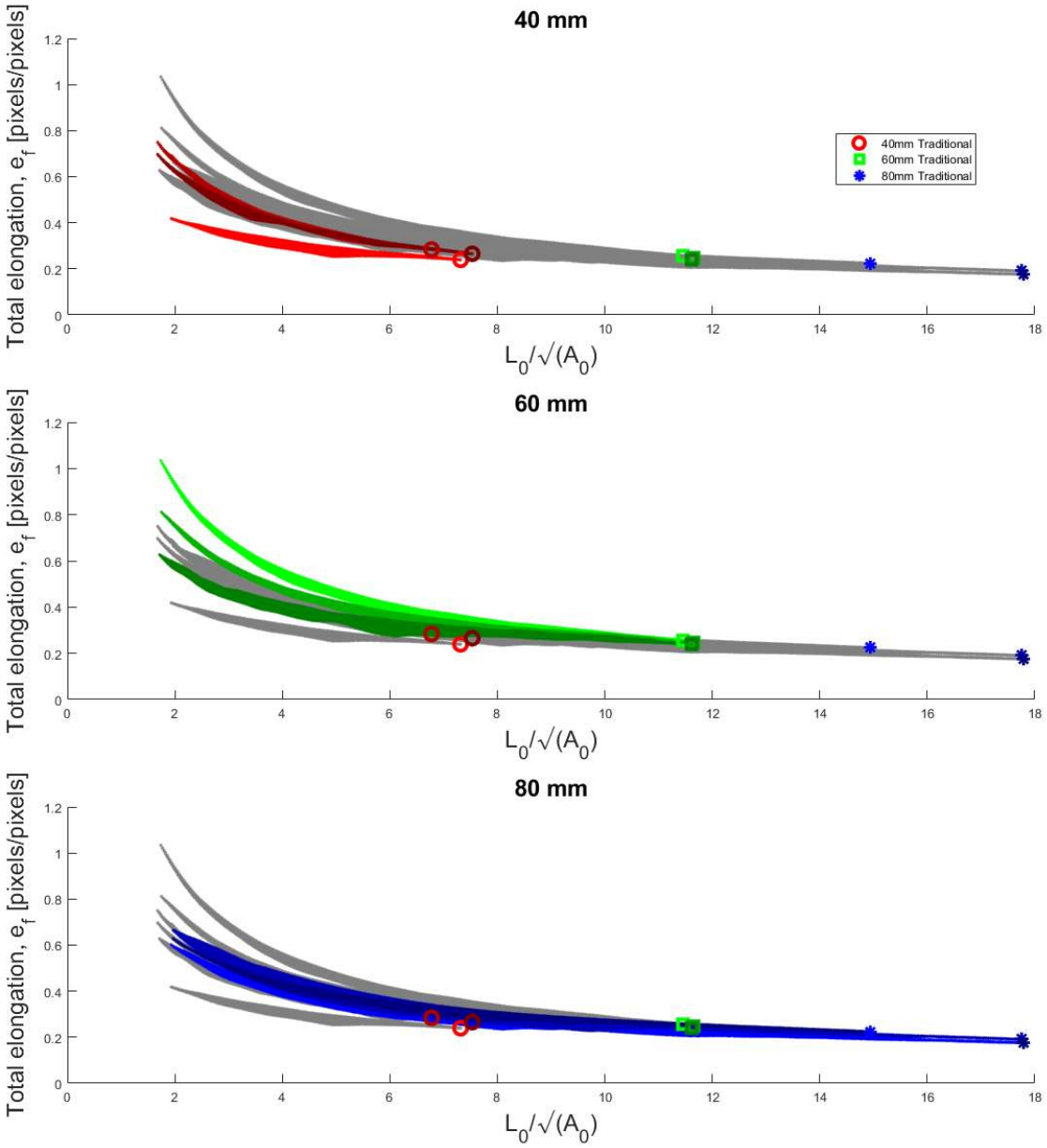

Figure 12. Extensometer values for each specimen tested plotted on similar axes with the fitted Unified Law overlayed. Each color is the three separate specimens of each gauge length plotted in different shades

4.3 Comparing the Laws

A plot summarizing the results is shown in Figure 12. The obtained value for each parameter of Barba's Law (Blue), Oliver's Law (Red), and the Unified Law (Yellow). The top row details the value for κ. The second row shows the value obtained for -α. The third row shows the value obtained for e_u. The columns are the values obtained from the 40 mm, 60 mm, 80 mm, and the combined data/non-variable extensometer values, respectively. A line detailing the mean value for each parameter across all the data is shown with color corresponding to the respective law. The -α value for each data set for Barba's Law is set to one and e_u for Oliver's Law is set to zero.

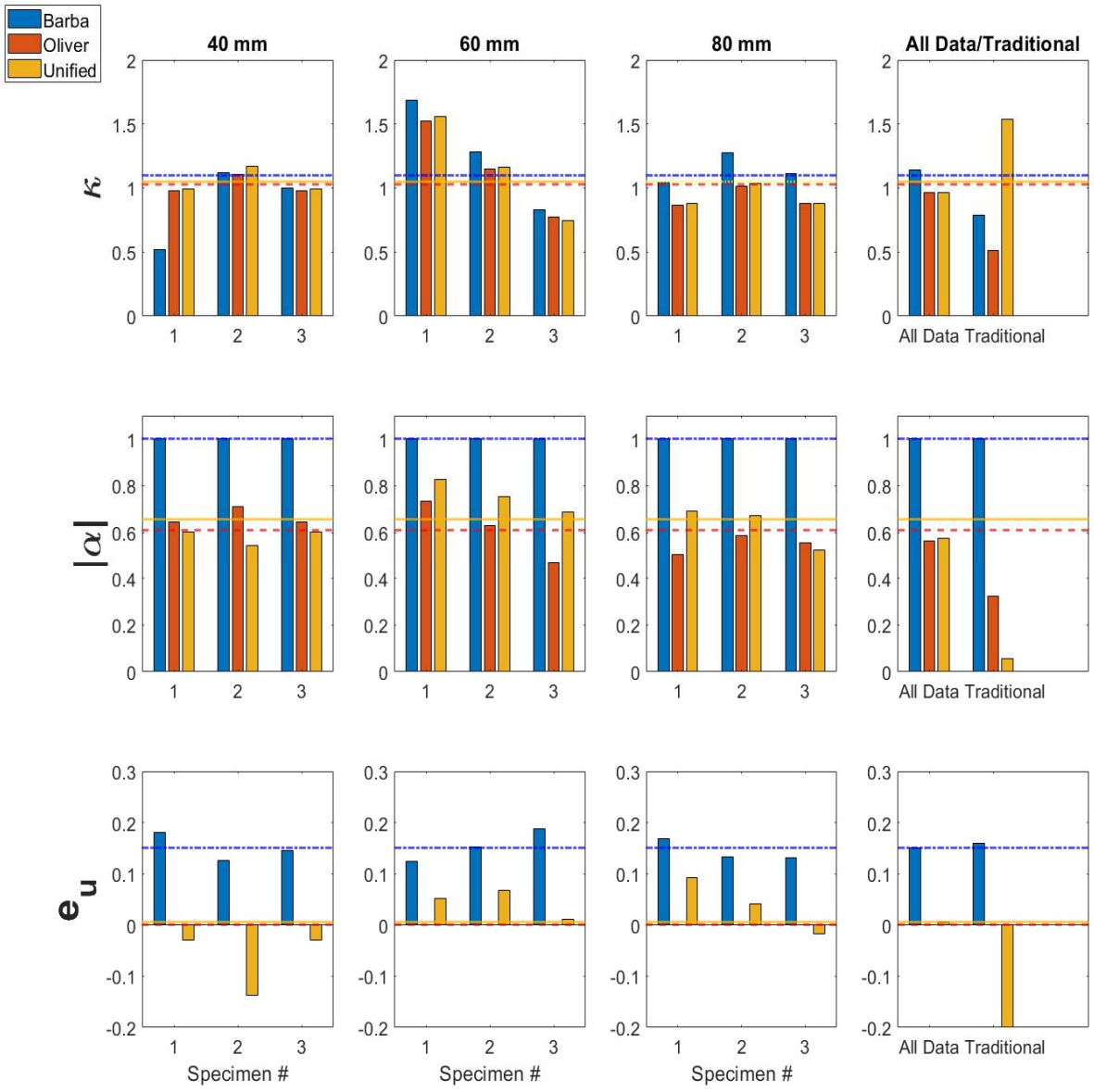

Figure 13. A plot detailing the obtained value for each parameter of Barba's Law (Blue), Oliver's Law (Red), and the Unified Law (Yellow). The top row details the value for κ. The second row shows the value obtained for -α. The third row shows the value obtained for e_u. The columns are the values obtained from the 40 mm, 60 mm, 80 mm, and the combined data/non-variable extensometer values, respectively. A line detailing the mean value for each parameter across specimens is shown with color corresponding to the respective law.

Specimens of the same geometry have variations between the values obtained. This gives an indication of the distribution that should be expected on a specimen to specimen basis. This is also seen in examination of Figure 12 where the differences of the extensometer values between specimens of the same geometry can be clearly seen. This variation between specimens of different geometries is comparable to the variation between specimens of the same geometries.

The data from the combined data set corresponds closely with the average across the specimens, meaning that distributions between individual parameters of each specimen is comparable to the distribution of the individual variation in variable extensometer data sets. This shows that the two different methods for averaging scaling parameters are comparable.

The κ values obtained are relatively comparable between laws and, on a specimen to specimen basis, tend to be tightly grouped. The $-\alpha$ values obtained between Oliver's Law and the Unified Law are closely grouped as well, but neither are near the value of one that was enforced in Barba's Law. This shows how Barba's Law is insufficient in capturing the curvature that exists in the data. The e_u values tend to show more variation than the other parameters. Barba's Law values are consistently positive, indicating that the un-necked portion of the specimen is in tension. The Unified Law produces both positive and negative values, indicating that the un-necked portion is sometimes in tension or compression, and the positive values were on average much lower than Barba's Law. The values of e_u obtained through the Unified Law average around zero

indicating that addition of e_u for the Unified Law may not provide a meaningful improvement over Oliver's Law.

Table 1: Ductility parameters taken from the combined data set, the traditional method, and the average across each individual specimen with the 95% confidence interval and R^2 reported

Law	Parameter	All Data		Traditional		Specimen Average	
		Value	95% Conf	Value	95% Conf	Value	95% Conf
Barba's	K	1.1405	0.0041	1.0963	0.0040	0.7914	1.0189
	e_u	0.1499	0.0007	0.2271	0.0008	0.1604	0.1026
	R^2	0.8181		0.6584		0.974	
Oliver's	K	0.9619	0.0033	1.0287	0.0024	0.5123	0.45498
	A	-0.5651	0.0018	-0.6088	0.0015	-0.3242	0.03761
	R^2	0.8295		0.7127		0.986	
Unified	K	0.9617	0.0122	1.0463	0.0049	1.5387	207.9674
	A	-0.5746	0.0122	-0.6557	0.012	-0.0579	9.0720
	e_u	0.0057	0.0072	0.0059	0.0074	-1.1028	210.1272
	R^2	0.829		0.712		0.98	

Table 1 shows the values, 95% confidence interval, and R^2 value for the combined data set and the non-variable extensometer method, and the data averaged across each individual specimen. Tables with the parameters for each individual specimen can be found in the Appendix.

A comparison between the individual specimen values and the traditional values clearly demonstrate the benefits of the variable extensometer method. The 95% confidence interval for each individual specimen does not exceed 10% of the measured value for any parameter. The 95% confidence interval for the traditional method is at best 10% of the measured value and at worst case is a much larger than the measured value. The R^2 values also demonstrate this. The R^2 value for any of the individual specimens are all above 0.95 indicating a good quality of fit. The R^2 value for the non-variable extensometer method was between 0.65 and 0.75 indicating a lower quality fit. The unified law for the non-variable extensometer method has both very high uncertainty values and a low R^2. This indicates that the Unified Law is not applicable to the traditional method. The addition of the extra parameter does not lend well to the small amount of available data points.

The modification made to the Unified Law was the addition of e_u. The average value obtained for e_u, shown in Table 1, is near zero. The average uncertainty is also greater than 100% of the measured value. The values obtained for e_u for the Unified Law showed a lot of variability between specimens. The 40 mm specimens produced all negative results. The 60 mm produced all positive results, and the 80 mm produced a mix. The concept of a negative e_u is not intuitive as it is indicating a compressive uniform elongation and, the positive values measured were much lower than the values measured from Barba's Law. This further indicates that the Unified Law may not introduce a measurable improvement over Oliver's Law, but it is still a useful analytical tool for comparing between Barba's and Oliver's Laws.

4.4 Comparison to Values in Literature

Figure 14 shows an Ashby-style plot of the Oliver's Law parameters (κ and α) from various sources, plotted with κ on the horizontal axis and α on the vertical axis. Although all the data is for low carbon steel, each reference uses a different alloy of steel. The 40 mm, 60 mm, and 80 mm entries represent the data obtained through this work described in the previous sections, with a black line drawn around them to indicate that they all come from the same material. The next 2 entries are values taken from Oliver's work. Series 1 is described as "best quality 1 ¾ inch mild-steel shafting" that was machined to diameters ranging from 0.35 inches to 1.35 inches. Series 2 is described as "1 ½ inch diameter Bessemer steel" that was machined to diameters ranging from 0.3 inches to 1.3 inches [26]. The next 3 entries come from the work performed by Dhalla and Winter [29,41]. Dhalla and Winter used several different types of low carbon steel that was characterized by their total elongation in a 2-inch gauge section that encompassed the neck. Low ductility was elongations ranging from 4.4 % to 5.3%. Medium Ductility ranged from 36.5% to 39.1%. High ductility ranged from 49.8% to 52.2 % [29,41]. Xu used X80 high strength steel samples that came from pipe, coil, and plate [28].

The figure shows variation of the Oliver's Law scaling parameters from specimen to specimen as well as the variation from alloy to alloy. Although each of these studies used low carbon steel, there can exist a large variation in chemical composition, microstructure, and other processing methods between each material, which can cause significant variation in mechanical properties. All the data shown in this figure is of comparable magnitude. Additionally, each data set with sufficient points shows a

distribution that is comparable or larger to the variation in the data shown for the 40 mm, 60 mm, and 80 mm used in this work.

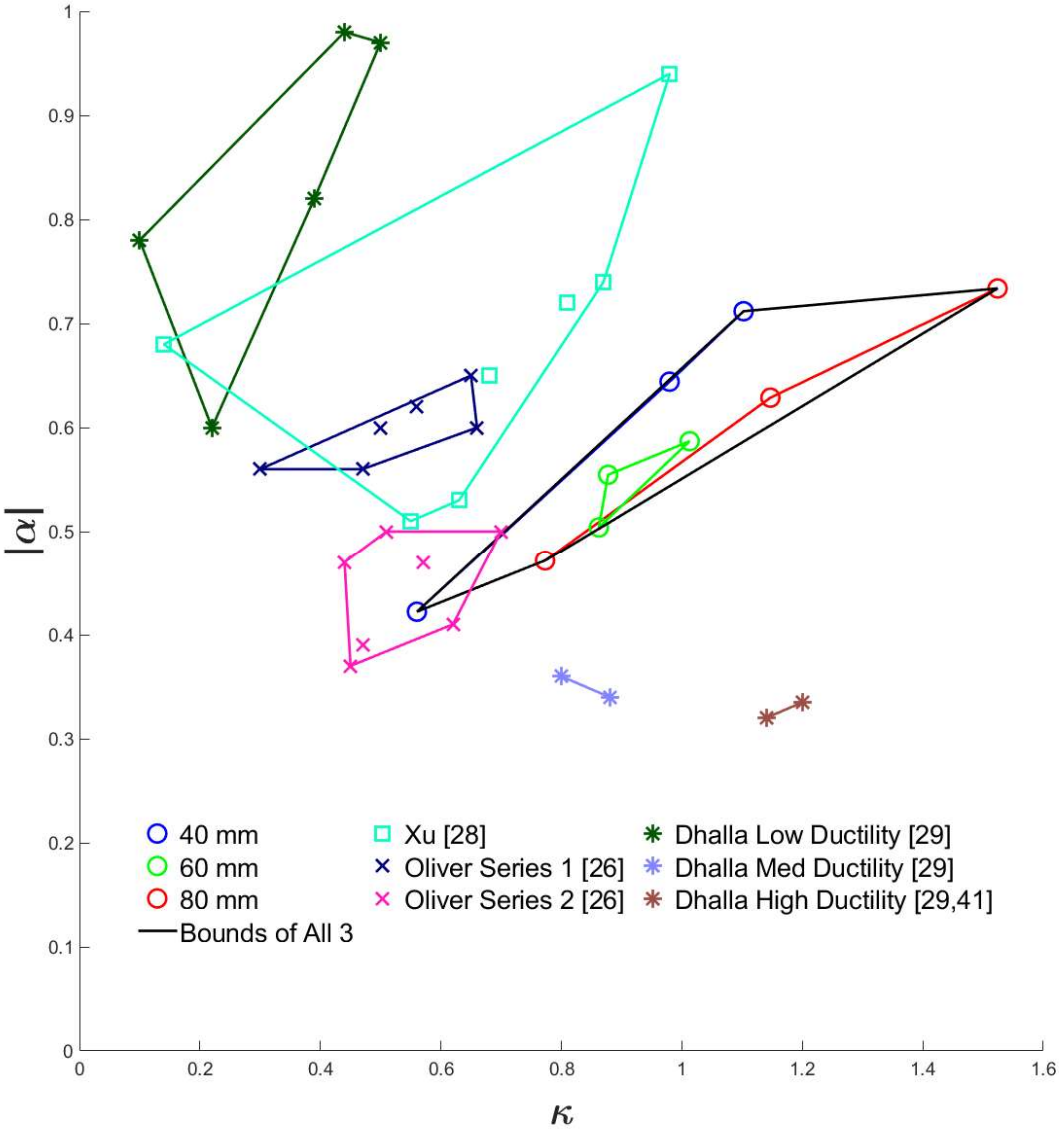

Figure 14. A plot comparing different Oliver's Law parameters from literature to values obtained in this work. The horizontal axis represents κ. The vertical axis represents negative α. Values obtained from literature are shown as markers and lines encompass the outer bounds of the data. Descriptions of each legend entry can be found in the accompanying text

CHAPTER 5

DISCUSSION

5.1 Scaling Parameters Over Time

One of the unique benefits of the variable extensometer method is that the variable extensometer values can be extracted from any image during a tension test. This gives the ability to monitor how these parameters develop overtime. Figure 15 shows the value for Barba's and Oliver's Law ductility parameters taken at every image during its tension test. The Gleeble collected measurements at 100 Hz and the image capture rate was 2 Hz. Often the specimen fractured between image capture that lead to inconsistent capturing final portion of the stress strain curve. Therefore, some curves may appear incomplete because the final specimen fracture occurred in between images.

Figure 15 shows how the ductility parameters κ, α, and e_u develop over the course of the tension test. The stress strain behavior between all specimens is very close with the main variation between specimen being the strain at which they failed. Feature A labels an inconsistency in one of the stress-strains curves caused by the specimen slipping in the grips early in the test. Feature B labels the Lüder's Band behavior, which will be discussed in further detail in section 5.2. All the curves displayed this behavior except for one 40 mm specimen. This one 40 mm specimen was the specimen with the lowest e_f values shown in the first row of Figure 12 and lowest scaling parameter values shown in the far left of the first column of Figure 13. Feature C highlights that all the 80 mm specimens failed at the lowest overall strain. This behavior is expected. The necked

portion in a longer specimen takes up less of the overall gauge length leading to less total strain. This reiterates the need for the scaling laws that can translate between geometries.

The behavior over time for the Barba's Law parameters generally agrees with intuition. Since e_u captures the uniform elongation, it is expected that it would increase linearly in proportion with the total strain until the onset of necking. Once necking has occurred, deformation is no longer uniform and the value plateaus at its final value. In Barba's Law, κ describes the necking behavior. Prior to necking, it should nominally be zero then upon the onset of necking would increase to its final value at fracture. All the specimens display this behavior. At the ultimate strength—where necking begins to occur—there is a sharp rise in κ and e_u begins to plateau. This plateau is marked by feature D.

Oliver's Law parameters are less physically intuitive. In Oliver's Law, κ describes the linear slope while α captures the curvature. So, during uniform deformation, these would both be nominally zero then increase upon the onset of necking. However, since Oliver's law does not include an e_u term to describe non-zero uniform deformation, both κ and α are found to be non-zero. Comparison of κ obtained for Barba's Law to κ obtained from Oliver's Law shows similar behavior. Figure 13 shows that there are small differences in the final value that they arrive at, but the behavior of the curves is similar. They both increase rapidly at the onset of necking. α also shows similar behavior where the slope of the curve is relatively low prior to the reaching the ultimate strength. There is an increase in the slope in the negative direction that corresponds with the change in the other parameters and the onset of necking.

Feature E labels some erratic behavior in the α parameter early in the test. At small—mostly elastic—strains of the tension test, the variable extensometers values form a relatively straight line with a random noise. Most of the parameters are immune to this noise, but being an exponential parameter, α is very sensitive. This causes large variations both positive and negative in α until the specimen has been sufficiently deformed and α displays more consistent, expected behavior. Oliver's Law was developed to characterize late stage ductility, not the elastic region of the stress strain curve, so this behavior is reasonable. The α plot has been cropped to a vertical axis ranging between -1 to +1 because the early variations can upset the scale of the graph and make it difficult to depict the late stage behavior.

While Figure 13 shows that the final value for the parameters between specimens is comparable, Figure 15 shows that the route that each specimen takes to get to the final value can be quite different. This indicates that the scaling laws and the variable extensometer method are useful in capturing proper scaling values while being path independent. This also furthers the concept that percent elongation is insufficient in capturing a materials ductility. Several specimens failed at different strain values yet ended up with comparable scaling parameters. This also shows that post-mortem analysis of the scaling laws will not fully characterize a specimen's behavior at all stages of a tension test.

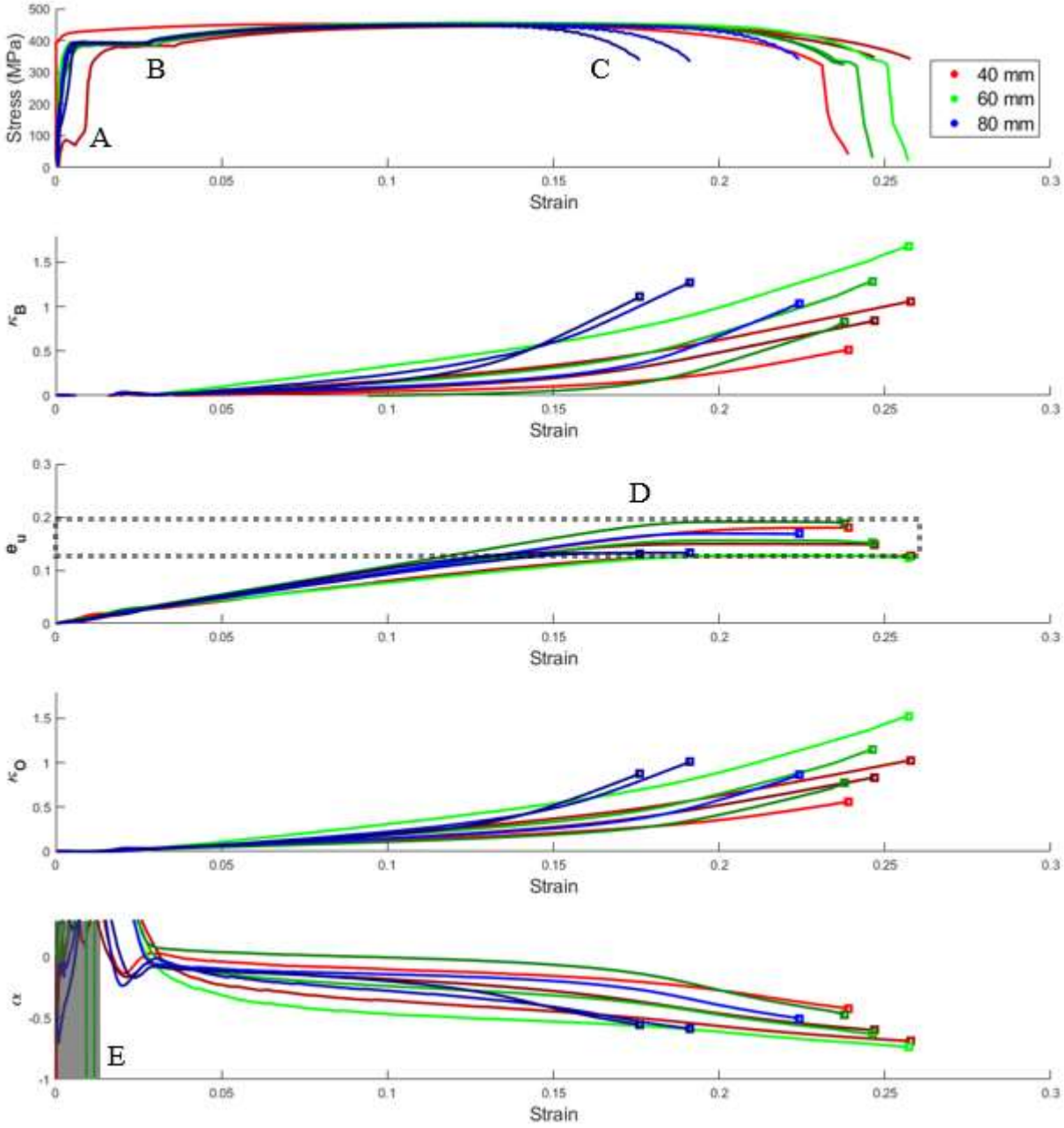

Figure 15. Barba's Law and Oliver's Law parameters development over the duration of a tension test for each specimen tested. Horizontal axis for each plot is strain the top row vertical axis shows stress, second row shows κ from Barba's Law, third shows e_u from Barba's Law, fourth shows κ from Oliver's Law and fifth shows α. 40 mm specimens are shown in different shade of red, 60 mm in shades of green, and 80 mm in shades of blue.Squares indicate the values taken for Figure 13. Labeled features are discussed in accompanying text. The α plot has been cropped to maintain an appropriate scale.

The Unified Law parameters over time can be seen in Figure 16. The same stress-strain curve seen in Figure 15 is shown on top. The second row is κ from the Unified Law. The third row is α from the Unified Law. The fourth row is e_u from the Unified Law. The three parameters used in the Unified Law curve fitting make all the parameters overall more sensitive to noise, especially prior to necking where Barba's, Oliver's, and the Unified Law are not meant to characterize. This can be seen clearly in Figure 16 where the curves become noticeably more consistent at the onset of necking until they reach their final value. As seen previously in Figure 13, the Unified Law parameters correspond closely to Oliver's Law parameters. So, it would be expected that the Unified Law would show similar behavior to Oliver's Law over time. However, the noise seen prior to necking makes it difficult to draw conclusions from the individual parameter behaviors over time, but it is clear that the Unified Law should not be used prior to the onset of necking.

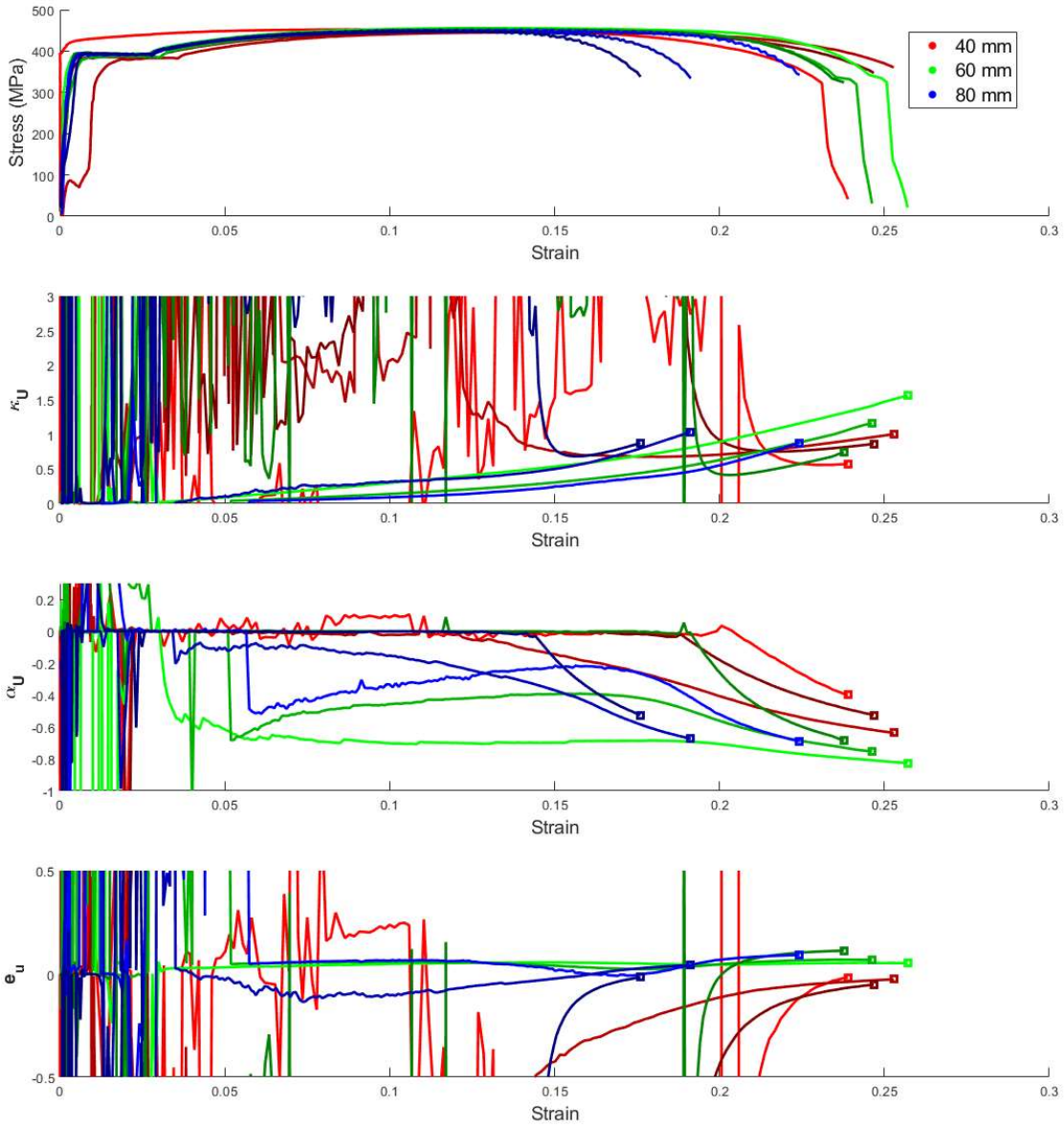

Figure 16. Unified Law parameters development over the duration of a tension test for each specimen tested. Horizontal axis for each plot is strain the top row vertical axis shows stress, second row shows κ from Barba's Law, third shows e_u from Barba's Law, fourth shows κ from Oliver's Law and fifth shows α. 40 mm specimens are shown in different shade of red, 60 mm in shades of green, and 80 mm in shades of blue. Squares indicate the values taken for Figure 13

5.2 Lüder's Band Behavior

Lüder's Bands (Feature B)—also known as slip bands—are inhomogeneous deformation bands that occur as a specimen transitions from elastic to plastic deformation. This is a well-known phenomenon that has been readily observed with several methods including DIC [42]. This phenomenon is not fully characterized, but it is related to dislocation motion early in a tensile test. Once a material hits its yield point there will be a stress plateau and the specimen will begin deforming non-uniformly as it transitions from elastic to plastic flow. This effect typically begins at the outer edges of the gauge lengths where internal stresses from the specimen shoulders is concentrated and works its way in bands to the center of the specimen. This work observed Lüder's Bands in 8 of the 9 tested specimens. An example of this observed in DIC on a 60 mm specimen is shown in Figure 17a. This figure first shows a uniform strain distribution. Then as the specimen begins yielding the strain works its way from the top and bottom of the specimen towards the center displaying the Lüder's Band effect.

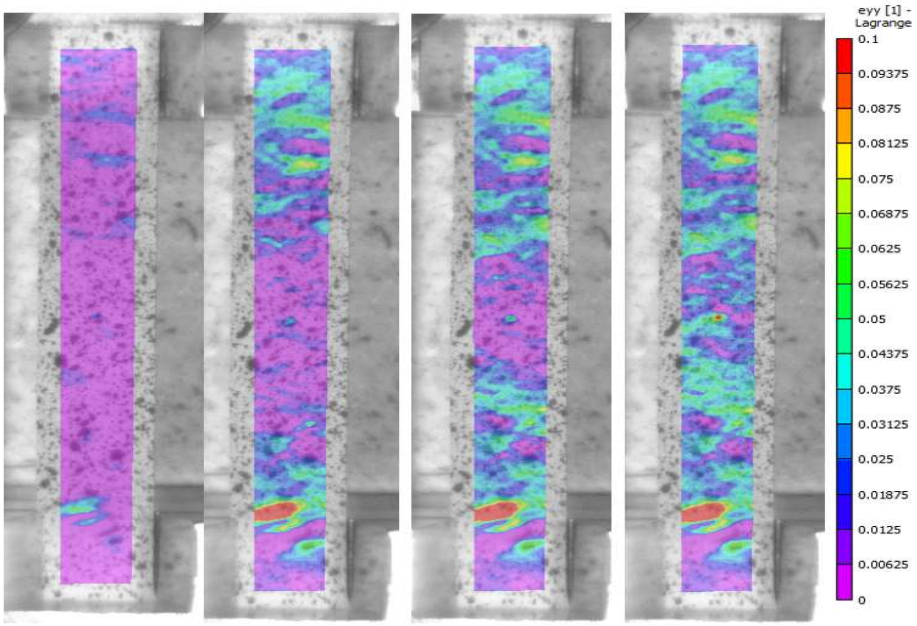

(a)

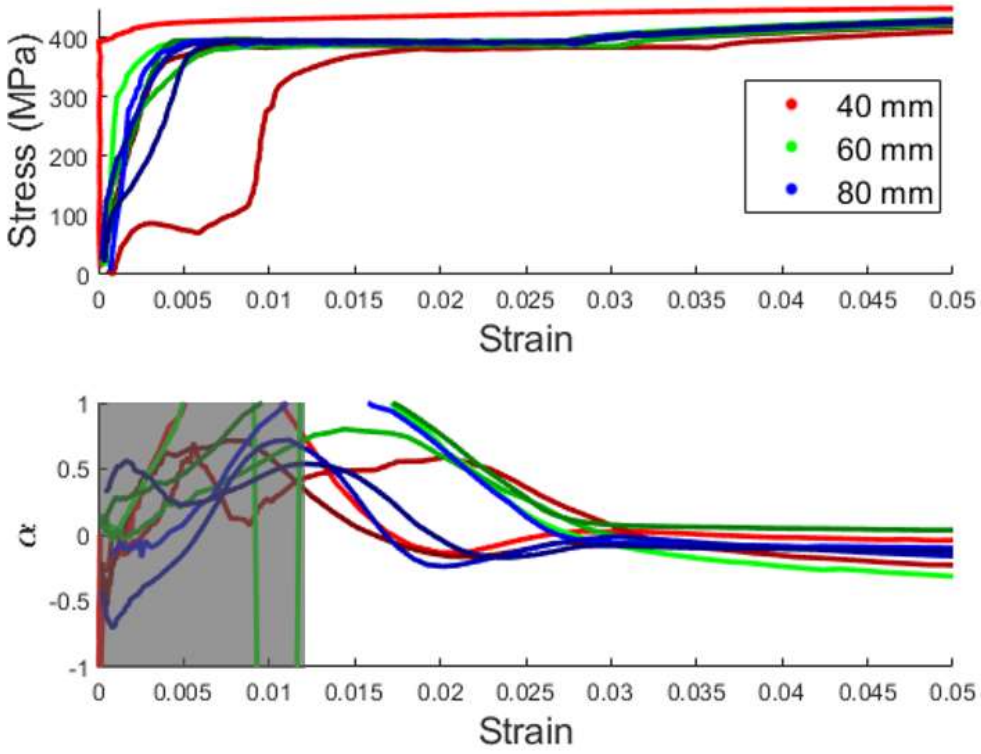

(b)

Figure 17. (a) Lüder's Bands observed in a 60 mm specimen. DIC strain contours in the vertical direction are shown overlayed on 4 consecutive images. (b) a cropped version of Figure 15 highlighting the Lüder's Band effect on the stress-strain curve and α. Area of high-uncertainty is marked in gray. 40 mm specimens are shown in different shade of red, 60 mm in shades of green, and 80 mm in shades of blue.

A cropped version of Figure 15 that highlights the stress-strain and α behavior during the effect is shown in Figure 17b. The Lüder's Band becomes obvious when examining the stress-strain behavior of each specimen where there is a prominent plateau in the stress-strain curve as the specimen yields and transitions from elastic to plastic deformation.

The strains and displacements where this effect occurs are much lower in magnitude compared to the final elongations taken from the variable extensometer method. However, Lüder's Bands are non-uniform deformation and some effect on the scaling parameters is expected. Both Barba's Law and Oliver's Law were designed to characterize necking which means that an extensometer value will encapsulate the non-uniformity in the center. Lüder's Bands occur in the opposite direction working from the outside toward the center. κ and e_u represent the slope and intercept of a line, respectively. Since the Lüder's Band is generally symmetric and occurs opposite to what the equations are meant to characterize, it would not affect either the slope or the intercept of the data and these parameters show no significant impact. However, the Lüder's Band effect would change the curvature of the displacement of the data as it traverses across the specimen which is what α is meant to characterize. So, across all the specimens that displayed the Lüder's Band effect, there was a measurable temporary change in α that happened in both the positive and negative direction depending on specimen. Neither Oliver's Law nor the variable extensometer method were designed to measure this effect, but their ability to detect the phenomena is interesting to note.

CHAPTER 6

CONCLUSIONS AND POTENTIAL FUTURE WORK

6.1 Summary

This work introduced a novel variable extensometer method to obtain ductility scaling parameters from single specimens. Using DIC, the variable extensometer extracts full-field, in-situ displacement measurements across the entire gauge length of the specimen. The full-field displacements are then used to down-select many shorter gauge lengths over which to compute elongation by $\Delta L/L_0$. The many gauge lengths are validated by also comparing variable extensometer measurements from specimens having three different physical lengths: 40, 60, and 80 mm.

This technique was shown to have several benefits. First, it allows for ductility scaling parameters (e.g. the fitting constants from Barba's and Oliver's Laws) to be extracted from a single specimen. Second, by computing elongation thousands of times from each specimen, it provides orders of magnitude more data than previous techniques which obtained one data point per failed specimen. Additionally, since the technique is performed in-situ, it is capable of extracting extensometer data and scaling parameters throughout the duration of a tension test, allowing for further understanding of all stages of a material's deformation behavior even prior to failure.

The variable extensometer technique allowed for further investigation of the two commonly used scaling laws: Barba's Law and Oliver's Law. A third, unified law was introduced as an analytical tool to compare between the two laws. This investigation

showed that, while Barba's Law contains the more physically intuitive parameter, e_u, it does not sufficiently characterize curvature seen in the data. Oliver's Law better captures curvature, but for long gauge lengths incorrectly converges to zero elongation instead of the more physically meaningful e_u. However, the addition of e_u to Oliver's Law did not yield any significant improvement over Oliver's Law in fitting the data.

6.2 Potential Future Work

This work demonstrated the ability of the variable extensometer method to characterize ductility at the macro-scale. However, further work is needed to apply the technique at micro- and nanoscales, which is under current investigation by our co-investigators at the University of Utah. Smaller length scales are especially interesting for characterizing irradiated materials, as miniaturized specimens require less irradiation dose to accumulate the same level of damage and are therefore much safer to handle and transport.

With the prevalence of micro/nano-scale ductility measurements, further work should be done to investigate the scaling laws at smaller length scales. SEM-based DIC has been shown to work at the nanoscale [43], but the applicability of the scaling laws used in this study at that scale is still unknown. Further investigation of the Unified, Oliver's, and Barba's Law should be performed using SEM-scale ductility specimens, which are currently in development at the University of Utah.

Finally, the variable extensometer method should be applied to characterize ductility at high temperature. During elevated temperature tests, there is often temperature non-uniformity in the gauge length due to the water-cooled grips. The

variable extensometer method makes it possible to select only the portion of the gauge region with an acceptably uniform temperature profile to explore the effect of temperature on ductility scaling parameters. Once the technique is demonstrated at high temperature, the long-term goal is to further apply it under combined high temperature and irradiated conditions.

REFERENCES

[1] Lister, D. H., 2012, "Understanding and Mitigating Corrosion in Nuclear Reactor Systems," *Nuclear Corrosion Science and Engineering*, Elsevier, pp. 57–74.

[2] 1986, *The Use of Small-Scale Specimens for Testing Irradiated Material: A Symposium Sponsored by ASTM Committee E-10 on Nuclear Technology and Applications, Albuquerque, N.M., 23 Sept. 1983*, Philadelphia, Pa.: ASTM.

[3] Kryukov, A., Debarberis, L., von Estorff, U., Gillemot, F., and Oszvald, F., 2012, "Irradiation Embrittlement of Reactor Pressure Vessel Steel at Very High Neutron Fluence," Journal of Nuclear Materials, **422**(1), pp. 173–177.

[4] Gussev, M. N., Howard, R. H., Terrani, K. A., and Field, K. G., 2017, "Sub-Size Tensile Specimen Design for in-Reactor Irradiation and Post-Irradiation Testing," Nuclear Engineering and Design, **320**, pp. 298–308.

[5] Kasada, R., Takayama, Y., Yabuuchi, K., and Kimura, A., 2011, "A New Approach to Evaluate Irradiation Hardening of Ion-Irradiated Ferritic Alloys by Nano-Indentation Techniques," Fusion Engineering and Design, **86**(9–11), pp. 2658–2661.

[6] Uchic, M. D., Dimiduk, D. M., Florando, J. N., and Nix, W. D., 2004, "Sample Dimensions Influence Strength and Crystal Plasticity," Science, **305**(5686), pp. 986–989.

[7] Ozdemir, N., Karaman, I., Mara, N. A., Chumlyakov, Y. I., and Karaca, H. E., 2012, "Size Effects in the Superelastic Response of Ni54Fe19Ga27 Shape Memory Alloy Pillars with a Two Stage Martensitic Transformation," Acta Materialia, **60**(16), pp. 5670–5685.

[8] Espinosa, H. D., Zhu, Y., and Moldovan, N., 2007, "Design and Operation of a MEMS-Based Material Testing System for Nanomechanical Characterization," Journal of Microelectromechanical Systems, **16**(5), pp. 1219–1231.

[9] Kang, W., and Saif, M. T. A., 2010, "A Novel Method for In Situ Uniaxial Tests at the Micro/Nano Scale—Part I: Theory," Journal of Microelectromechanical Systems, **19**(6), pp. 1309–1321.

[10] Kang, W., Han, J. H., and Saif, M. T. A., 2010, "A Novel Method for In Situ Uniaxial Tests at the Micro/Nanoscale—Part II: Experiment," Journal of Microelectromechanical Systems, **19**(6), pp. 1322–1330.

[11] Oliver, W. C., and Pharr, G. M., 1992, "An Improved Technique for Determining Hardness and Elastic Modulus Using Load and Displacement Sensing Indentation Experiments," Journal of materials research.

[12] Oliver, W. C., and Pharr, G. M., 2004, "Measurement of Hardness and Elastic Modulus by Instrumented Indentation: Advances in Understanding and Refinements to Methodology," Journal of Materials Research, **19**(1), pp. 3–20.

[13] Ohmori, M., and Wakasa, K., 1973, "TENSILE DUCTILITY OF COPPER AND Alpha -BRASS SINGLE CRYSTALS AT ELEVATED TEMPERATURES.," Nippon Kinzoku Gakkaishi/Journal of the Japan Institute of Metals, **37**, pp. 1195–1199.

[14] Zhao, Y. H., Guo, Y. Z., Wei, Q., Dangelewicz, A. M., Xu, C., Zhu, Y. T., Langdon, T. G., Zhou, Y. Z., and Lavernia, E. J., 2008, "Influence of Specimen Dimensions on the Tensile Behavior of Ultrafine-Grained Cu," Scripta Materialia, **59**(6), pp. 627–630.
[15] Sun, J., Jin, L., Dong, J., Wang, F., Dong, S., Ding, W., and Luo, A. A., 2019, "Towards High Ductility in Magnesium Alloys - The Role of Intergranular Deformation," International Journal of Plasticity, **123**, pp. 121–132.
[16] Kassner, M. E., Nguyen, N. Q., Henshall, G. A., and McQueen, H. J., 1991, "The Effects of Temperature and Strain Rate on Extended Ductility of Aluminum," Materials Science and Engineering: A, **132**, pp. 97–105.
[17] Laporte, V., and Mortensen, A., 2009, "Intermediate Temperature Embrittlement of Copper Alloys," International Materials Reviews, **54**(2), pp. 94–116.
[18] "Mechanical Behavior of Materials: Thomas H. Courtney: 9781577664253: Amazon.Com: Books" [Online]. Available: https://www.amazon.com/Mechanical-Behavior-Materials-Thomas-Courtney/dp/1577664256. [Accessed: 26-Aug-2020].
[19] Porollo, S. I., Dvoryashin, A. M., Ivanov, A. A., Konobeev, Yu. V., and Shulepin, S. V., 2019, "Study of Phase-Structural Transformations Resulting in Low-Temperature Radiation Embrittlement in Ferritic-Martensitic Steel," Atomic Energy, **126**(1), pp. 39–45.
[20] Takeda, Y., Kiattisaksri, C., Aramaki, M., Munetoh, S., and Furukimi, O., 2017, "Effects of Specimen Thickness in Tensile Tests on Elongation and Deformation Energy for Industrially Pure Iron," ISIJ International, **57**(6), pp. 1129–1137.
[21] Sergueeva, A. V., Zhou, J., Meacham, B. E., and Branagan, D. J., 2009, "Gage Length and Sample Size Effect on Measured Properties during Tensile Testing," Materials Science and Engineering: A, **526**(1), pp. 79–83.
[22] Sun, X., Soulami, A., Choi, K. S., Guzman, O., and Chen, W., 2012, "Effects of Sample Geometry and Loading Rate on Tensile Ductility of TRIP800 Steel," Materials Science and Engineering: A, **541**, pp. 1–7.
[23] Yuan, W. J., Zhang, Z. L., Su, Y. J., Qiao, L. J., and Chu, W. Y., 2012, "Influence of Specimen Thickness with Rectangular Cross-Section on the Tensile Properties of Structural Steels," Materials Science and Engineering: A, **532**, pp. 601–605.
[24] Hogström, P., Ringsberg, J. W., and Johnson, E., 2009, "An Experimental and Numerical Study of the Effects of Length Scale and Strain State on the Necking and Fracture Behaviours in Sheet Metals," International Journal of Impact Engineering, **36**(10), pp. 1194–1203.
[25] Dieter, G., 1986, *Mechanical Metallurgy*, McGraw-Hill Education, New York.
[26] Oliver, D. A., 1928, "Proposed New Criteria of Ductility from a New Law Connecting the Percentage Elongation with Size of Test-Piece," Proceedings of the Institution of Mechanical Engineers, **115**(1), pp. 827–864.
[27] 14:00-17:00, "ISO 2566-1:1984," ISO [Online]. Available: https://www.iso.org/cms/render/live/en/sites/isoorg/contents/data/standard/00/75/7524.html. [Accessed: 14-Sep-2020].
[28] Xu, X., Zhao, X., Ai, Y., Liang, M., Li, N., Lin, W., and Qin, C., 2020, "Study and Analysis on the Tensile Test Elongation Variation Law for High-Strength Pipeline Steel," J. of Materi Eng and Perform, **29**(4), pp. 2164–2171.

[29] Dhalla, A. K., and Winter, G., "Ductility Criteria and Performance of Low Ductility Steels for Cold-Formed Members," p. 10.
[30] Goltsev, V. Y., Degadnikova, L. A., and Osintsev, A. V., 2017, "The Mechanical Testing of Materials Using the Method of Digital Image Correlation," KnE Materials Science, pp. 124–132.
[31] Hild, F., and Roux, S., 2006, "Digital Image Correlation: From Displacement Measurement to Identification of Elastic Properties – a Review," Strain, **42**(2), pp. 69–80.
[32] Michael A., M. A., Orteu, J.-J., and Schreier, H. W., 2009, "Digital Image Correlation (DIC)," *Image Correlation for Shape, Motion and Deformation Measurements: Basic Concepts,Theory and Applications*, H. Schreier, J.-J. Orteu, and M.A. Sutton, eds., Springer US, Boston, MA, pp. 1–37.
[33] Jones, I., 2018, "A Good Practices Guide for Digital Image Correlation."
[34] Reu, P., 2012, "Introduction to Digital Image Correlation: Best Practices and Applications," Exp Tech, **36**(1), pp. 3–4.
[35] Crammond, G., Boyd, S. W., and Dulieu-Barton, J. M., 2013, "Speckle Pattern Quality Assessment for Digital Image Correlation," Optics and Lasers in Engineering, **51**(12), pp. 1368–1378.
[36] Lane, C., Burguete, R. L., and Shterenlikht, A., 2008, "An Objective Criterion for the Selection of an Optimum DIC Pattern and Subset Size," Experimental and applied mechanics, SEM ANNUAL CONFERENCE AND EXPOSITION OF EXPERIMENTAL AND APPLIED MECHANICS.
[37] Pan, B., Xie, H., Wang, Z., Qian, K., and Wang, Z., 2008, "Study on Subset Size Selection in Digital Image Correlation for Speckle Patterns," Opt. Express, OE, **16**(10), pp. 7037–7048.
[38] Kwak, J. B., 2019, "Completely in Situ and Non-Contact Warpage Assessment Using 3D DIC with Virtual Patterning Method," International Journal of Advanced Manufacturing Technology, **100**(9–12), pp. 2803–2811.
[39] Croom, B., Wang, W.-M., Li, J., and Li, X., 2016, "Unveiling 3D Deformations in Polymer Composites by Coupled Micro X-Ray Computed Tomography and Volumetric Digital Image Correlation," Exp Mech, **56**(6), pp. 999–1016.
[40] Salzbrenner, B. C., Rodelas, J. M., Madison, J. D., Jared, B. H., Swiler, L. P., Shen, Y.-L., and Boyce, B. L., 2017, "High-Throughput Stochastic Tensile Performance of Additively Manufactured Stainless Steel," Journal of Materials Processing Technology, **241**, pp. 1–12.
[41] Dhalla, A. K., Winter, G., and Errera, S. J., "Influence of Ductility on the Structural Behavior of Light-Gage Cold-Formed Steel Members," p. 255.
[42] Brlić, T., Rešković, S., Vodopivec, F., and Jandrlić, I., 2018, "Lüders Bands at the Beginning of the Plastic Flow of Materials," Metalurgija, **57**(4), pp. 357–359.
[43] Kammers, A. D., and Daly, S., 2013, "Digital Image Correlation under Scanning Electron Microscopy: Methodology and Validation," Exp Mech, **53**(9), pp. 1743–1761.

APPENDIX

Table 1: Ductility parameters extracted for each specimen with the 95% confidence and R^2 value reported from the Matlab fit function

Specimen		40: 1		40: 2		40: 3	
		Value	95% Confidence	Value	95% Confidence	Value	95% Confidence
Barba's	κ	0.5165	0.0068	1.1217	0.0056	1.0018	0.0042
	e_u	0.1799	0.0016	0.1267	0.0015	0.1458	0.0011
	R^2	0.927		0.9903		0.9894	
Oliver	κ	0.9796	0.0025	1.1025	0.0034	0.9796	0.0025
	alpha	-0.6441	0.0018	-0.7118	0.0024	-0.6441	0.0018
	R^2	0.9947		0.9954		0.9947	
Unified	kappa	0.9923	0.0061	1.1715	0.013	0.9923	0.0061
	alpha	-0.6014	0.016	-0.5445	0.0188	-0.6014	0.016
	e_u	-0.0294	0.0117	-0.1375	0.02	-0.029	0.0117
	R^2	0.9948		0.9962		0.9948	

Specimen		60:1		60:2		60:3	
		Value	95% Confidence	Value	95% Confidence	Value	95% Confidence
Barba's	κ	1.6821	0.0028	1.2852	0.003	0.8319	0.0039
	e_u	0.1242	0.00050678	0.1522	0.0005363	0.883	0.0007
	R^2	0.9951		0.9903		0.9593	
Oliver	κ	1.5241	0.0024	1.147	0.0022	0.7729	0.0027
	alpha	-0.7337	0.00093946	-0.6287	0.0011	-0.4715	0.002
	R^2	0.9964		0.993		0.9623	
Unified	κ	1.5588	0.0035	1.1633	0.0031	0.7464	0.0037
	alpha	-0.8256	0.0054	-0.7531	0.0075	-0.6869	0.0178
	e_u	0.0526	0.0027	0.0682	0.0034	0.0119	0.0064
	R^2	0.9969		0.9939		0.9649	

Specimen		80:1		80:2		80:3	
		Value	95% Confidence	Value	95% Confidence	Value	
Barba's	κ	1.041	0.0027	1.277	0.0036	1.1097	0.0039
	eu	0.1681	0.00039137	0.1325	0.000459	0.1316	0.0007
	R2	0.9831		0.9706		0.9596	
Oliver	κ	0.8622	0.0017	1.0132	0.0026	0.8776	0.0027
	alpha	-0.504	0.001	-0.5869	0.0012	-0.5546	0.002
	R2	0.9874		0.9788		0.9773	
Unified	κ	0.8778	0.0029	1.038	0.0043	0.8767	0.0037
	alpha	-0.6901	0.0077	-0.6731	0.0082	-0.5255	0.0178
	eu	0.0917	0.0028	0.0415	0.0034	-0.0166	0.0064
	R2	0.9897		.9668		0.9774	